

UC Berkeley

UC Berkeley Previously Published Works

Title

Low-Voltage Magnetoelectric Coupling in $\text{Fe}_{0.5}\text{Rh}_{0.5}/0.68\text{PbMg}_{1/3}\text{Nb}_{2/3}\text{O}_3-0.32\text{PbTiO}_3$ Thin-Film Heterostructures

Permalink

<https://escholarship.org/uc/item/02g5g21v>

Journal

Advanced Functional Materials, 31(40)

ISSN

1616-301X

Authors

Zhao, Wenbo
Kim, Jieun
Huang, Xiaoxi
[et al.](#)

Publication Date

2021-10-01

DOI

10.1002/adfm.202105068

Peer reviewed

Low-Voltage Magnetoelectric Coupling in $\text{Fe}_{0.5}\text{Rh}_{0.5}/0.68\text{PbMg}_{1/3}\text{Nb}_{2/3}\text{O}_3\text{-}0.32\text{PbTiO}_3$ Thin-Film Heterostructures

Wenbo Zhao, Jieun Kim, Xiaoxi Huang, Lei Zhang, David Pesquera, Gabriel A. P. Velarde, Tanay Gosavi, Chia-Ching Lin, Dmitri E. Nikonov, Hai Li, Ian A. Young, Ramamoorthy Ramesh, and Lane W. Martin*

The rapid development of computing applications demands novel low-energy consumption devices for information processing. Among various candidates, magnetoelectric heterostructures hold promise for meeting the required voltage and power goals. Here, a route to low-voltage control of magnetism in 30 nm $\text{Fe}_{0.5}\text{Rh}_{0.5}/100$ nm $0.68\text{PbMg}_{1/3}\text{Nb}_{2/3}\text{O}_3\text{-}0.32\text{PbTiO}_3$ (PMN-PT) heterostructures is demonstrated wherein the magnetoelectric coupling is achieved via strain-induced changes in the $\text{Fe}_{0.5}\text{Rh}_{0.5}$ mediated by voltages applied to the PMN-PT. We describe approaches to achieve high-quality, epitaxial growth of $\text{Fe}_{0.5}\text{Rh}_{0.5}$ on the PMN-PT films and, a methodology to probe and quantify magnetoelectric coupling in small thin-film devices via studies of the anomalous Hall effect. By comparing the spin-flop field change induced by temperature and external voltage, the magnetoelectric coupling coefficient is estimated to reach $\approx 7 \times 10^{-8}$ s m^{-1} at 325 K while applying a -0.75 V bias.

1. Introduction

Moore's Law^[1] and Dennard scaling^[2] have been important guiding principles in the semiconductor industry. With the continued decrease of critical dimensions in logic and memory devices, however, there has been an increasing challenge to meet the requirements of these guiding principles, raising important challenges for the future of integrated circuit (IC) design.^[3] The strong desire to identify beyond-CMOS devices and technologies^[4-6] has driven increasing attention to a range of alternative computing platforms, including systems based on electron,^[7-9] spin,^[10,11] ferroelectric,^[12] strain,^[13] and other phenomena to overcome the "Boltzmann Tyranny" in electronic systems.^[14] Spin-based logic has emerged as one of the leading options^[4,6] due to an intriguing

combination of non-volatility, higher logic efficiency,^[15] and the potential for built-in memory-in-logic and/or logic-in-memory function. Traditional spin-logic devices, however, have limitations—including large energy dissipation during current-driven magnetic field or spin-transfer torque generation and that the fast spin decoherence of many semiconductors results from spin-orbit coupling.^[16]

Recently, a magnetoelectric spin-orbit (MESO) logic-in-memory device has been proposed to address these challenges.^[17] Taking advantage of the fact that a charge input/output is easier to accomplish, the input signal in the MESO device is a voltage input that is converted by the magnetoelectric into a spin signal. After the logic operations are completed in the spin domain, the spin is then back-converted to a charge signal using the inverse spin Hall effect.^[17] For the magnetoelectric module, three mechanisms have been proposed to accomplish the required function: strain, exchange coupling, or charge-induced effects.^[18-25] Each of these presents advantages and drawbacks; for example, exchange bias coupling of the magnetoelectric to a ferromagnet implicitly breaks time reversal symmetry but is an interface mediated coupling mechanism wherein controlling the strength of the coupling becomes non-trivial. In contrast, strain mediated approaches are longer range, but have the disadvantage of not breaking time symmetry and


Dr. W. Zhao, Dr. J. Kim, X. Huang, Dr. L. Zhang, Dr. D. Pesquera, Dr. G. A. P. Velarde, Prof. R. Ramesh, Prof. L. W. Martin
Department of Materials Science and Engineering
University of California
Berkeley, Berkeley, CA 94720, USA
E-mail: lwmartin@berkeley.edu

Dr. D. Pesquera
Catalan Institute of Nanoscience and Nanotechnology (ICN2)
CSIC and BIST
Campus UAB, Bellaterra, Barcelona 08193, Spain

Dr. T. Gosavi, Dr. C.-C. Lin, Dr. D. E. Nikonov, Dr. H. Li, Dr. I. A. Young
Components Research
Intel Corporation
Hillsboro, OR 97124, USA

Prof. R. Ramesh
Department of Physics
University of California
Berkeley, Berkeley, CA 94720, USA

Prof. R. Ramesh, Prof. L. W. Martin
Materials Sciences Division
Lawrence Berkeley National Laboratory
Berkeley, CA 94720, USA

 The ORCID identification number(s) for the author(s) of this article can be found under <https://doi.org/10.1002/adfm.202105068>.

DOI: 10.1002/adfm.202105068

hence are used to manipulate the magnetic anisotropy. Compared with the two other approaches, strain in composite heterostructures provides the potential for robust coupling in thick, large-area devices,^[18,22,26] and has made this approach more attractive. Numerous studies have explored the potential for magnetoelectric coupling in ferromagnetic/piezoelectric heterostructures including Co / 0.7PbMg_{1/3}Nb_{2/3}O₃-0.3PbTiO₃,^[27,28] Co_{0.4}Fe_{0.4}B_{0.2} / 0.7PbMg_{1/3}Nb_{2/3}O₃-0.3PbTiO₃,^[19,29] Fe_{0.5}Rh_{0.5} / 0.72PbMg_{1/3}Nb_{2/3}O₃-0.28PbTiO₃,^[22] etc. These works, however, made use of bulk or thick-film piezoelectrics which require high voltages (typically >250 V, corresponding to 5 kV cm⁻¹ for 0.5 mm thick piezoelectrics) and, thus large energies, to actuate; falling short of the growing call for low-power, energy-efficient devices.^[30]

Here, magnetoelectric coupling is explored in epitaxial multiferroic heterostructures of 30 nm Fe_{0.5}Rh_{0.5} / 100 nm 0.68PbMg_{1/3}Nb_{2/3}O₃-0.32PbTiO₃ (PMN-PT) and 30 nm Fe_{0.5}Rh_{0.5} / 10 nm MgO / 100 nm PMN-PT / 25 nm Ba_{0.5}Sr_{0.5}RuO₃ (BSRO) / NdScO₃ (NSO) (110) heterostructures. The thin MgO-buffer layer was employed to protect the PMN-PT thin films during high-temperature Fe_{0.5}Rh_{0.5} deposition in reducing conditions. It is found that high-quality, epitaxial, (001)-oriented films of Fe_{0.5}Rh_{0.5} can be grown on the PMN-PT thin films on both substrates. Subsequent temperature-dependent magnetization and resistivity studies reveal the ability to produce near-room-temperature phase transitions in the Fe_{0.5}Rh_{0.5}. A methodology to probe and quantify the magnetoelectric coupling in small thin-film devices via anomalous Hall effect studies is presented wherein one can compare the

spin-flop field change induced by temperature and external voltage to extract a measure of the magnetoelectric coupling coefficient. Values approaching $\approx 7 \times 10^{-8}$ s m⁻¹ at 325 K while applying just -0.75 V bias are achieved. The results demonstrate the potential for near room temperature low-voltage control of magnetism in Fe_{0.5}Rh_{0.5} via piezoelectric strain in PMN-PT thin films. Future directions and possible improvements to these devices are also discussed.

2. Results and Discussion

Here, we focus on using Fe_{0.5}Rh_{0.5} to demonstrate the potential for strain-mediated magnetoelectric coupling. This material has received considerable attention as a potential candidate for electrical-field control of magnetization due to its metamagnetic transition from an antiferromagnetic (AFM) phase to a ferromagnetic (FM) phase around $T^* \approx 350$ K.^[31-33] Previous studies demonstrated that epitaxial Fe_{0.5}Rh_{0.5} thin films can be grown on single-crystal substrates of piezoelectrics such as BaTiO₃ and PMN-PT and that field-induced strains from the substrates were able to shift the AFM-to-FM phase transition and induce large electroresistance effects.^[18,22] Here, we explored the optimization of Fe_{0.5}Rh_{0.5} growth in three heterostructure variants: 2 nm Pt / 30 nm Fe_{0.5}Rh_{0.5} / MgO (001) (henceforth, Fe_{0.5}Rh_{0.5}/MgO; Figure 1a), 2 nm Pt / 30 nm Fe_{0.5}Rh_{0.5} / 100 nm PMN-PT / 25 nm Ba_{0.5}Sr_{0.5}RuO₃ / NdScO₃ (110) (henceforth, Fe_{0.5}Rh_{0.5}/PMN-PT; Figure 1b), and 2 nm Pt / 30 nm Fe_{0.5}Rh_{0.5} / 10 nm MgO / 100 nm PMN-PT / 25 nm Ba_{0.5}Sr_{0.5}RuO₃ /

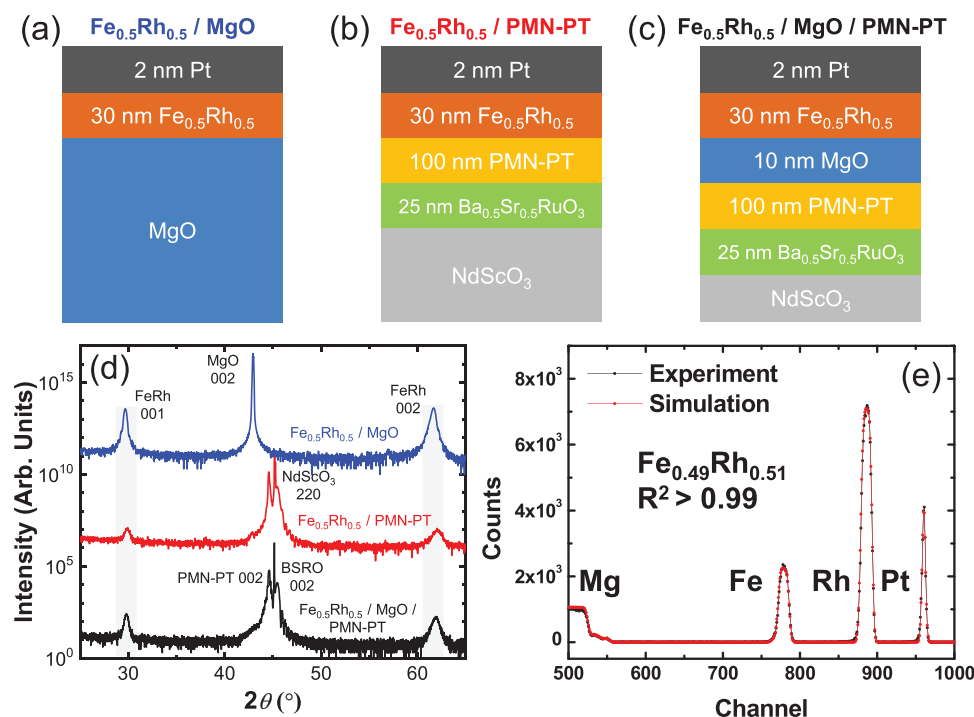


Figure 1. Schematic illustrations of the three heterostructure variants used and described in this work including the a) Fe_{0.5}Rh_{0.5}/MgO, b) Fe_{0.5}Rh_{0.5}/PMN-PT, and c) Fe_{0.5}Rh_{0.5}/MgO/PMN-PT structures. d) θ -2 θ X-ray diffraction scans for the same three heterostructure variants revealing the ability to produce fully epitaxial, 00l-oriented films of Fe_{0.5}Rh_{0.5} in all cases. e) Rutherford backscattering spectrometry spectra for an as-grown Fe_{0.5}Rh_{0.5}/MgO heterostructure at the optimized growth condition.

NdScO₃ (110) (henceforth, Fe_{0.5}Rh_{0.5}/MgO/PMN-PT; Figure 1c). Growth on MgO (001) substrates was used for internal reference due to the excellent lattice matching between Fe_{0.5}Rh_{0.5} (body-centered cubic, *a* = 0.423 nm) and MgO (rock-salt structure, *a* = 0.421 nm) and prior works showing that high-quality films can be produced therein.^[18,22] Details of the growth optimization are provided (Experimental Section; and Figure S1, Supporting Information). The PMN-PT films were produced following conditions established in previous studies using pulsed-laser deposition.^[34,35] The insertion of the MgO-buffer layer was explored in case the growth of the Fe_{0.5}Rh_{0.5} adversely effected the properties of the PMN-PT. Multiple thicknesses of MgO-buffer layer were explored (3–10 nm; data for growth on 3 nm MgO is also provided; Figure S2, Supporting Information), and it was found that the slightly thicker MgO layers provided for a better template layer upon which to produce high-quality Fe_{0.5}Rh_{0.5}, likely due to improved interface qualities from better lattice matching on thicker MgO layers. Following growth, the films were transferred to an ultrahigh vacuum sputter deposition system for the platinum and Fe_{0.5}Rh_{0.5} deposition at high temperatures. In all cases, it was found that high-quality, epitaxial (00*l*)-oriented Fe_{0.5}Rh_{0.5} films could be produced with the best results corresponding to growth at 600 °C (Experimental Section, Figure 1d). Estimates of the Fe_{0.5}Rh_{0.5} quality and ordering can be obtained by comparing the diffraction intensity for the 001- and 002-diffraction conditions,^[36] and via this analysis the Fe_{0.5}Rh_{0.5}/PMN-PT heterostructures were found to be as good or better than the Fe_{0.5}Rh_{0.5}/MgO heterostructures (Figure S3, Supporting Information). Subsequent studies of film stoichiometry

via Rutherford backscattering spectrometry (Experimental Section) indicate that the films grown at the optimized conditions have chemistry Fe_{0.49}Rh_{0.51} (Figure 1e), within error, the same as the source target and provided an expected AFM-to-FM phase transition at ≈350 K.^[31,32]

Having established the ability to create high-quality, epitaxial Fe_{0.5}Rh_{0.5}/PMN-PT heterostructures, we proceeded to explore the magnetic and transport properties as a function of temperature to further gauge the quality of the magnetic layer. Magnetization and resistivity (*ρ*) studies as a function of temperature show the expected first-order phase transition behavior for all heterostructures (Figure 2), consistent with previous reports.^[18,22] For the Fe_{0.5}Rh_{0.5}/MgO heterostructures, the AFM-to-FM phase transition occurs from 280–380 K (mid-point ≈330 K) with a hysteresis that is ~40 K wide at the mid-point (Figure 2a,b). At temperatures below ~250 K, the magnetization is essentially zero, indicating that the Fe_{0.5}Rh_{0.5} has been fully transformed to the AFM phase. This is accompanied by a change in the resistivity for the material (Figure 2b). These Fe_{0.5}Rh_{0.5}/MgO heterostructures compare favorably to similar structures reported in the literature and suggest we have high quality Fe_{0.5}Rh_{0.5} under the optimized growth conditions (Figure S4, Supporting Information). For the Fe_{0.5}Rh_{0.5}/PMN-PT heterostructures, the larger lattice mismatch between the Fe_{0.5}Rh_{0.5} and potential instability of the PMN-PT to high-temperature growth in reducing environments is found to be detrimental for the manifestation of idealized magnetic and transport properties (Figure 2c,d). Although no impurity phases were detected from X-ray diffraction, the magnetization studies

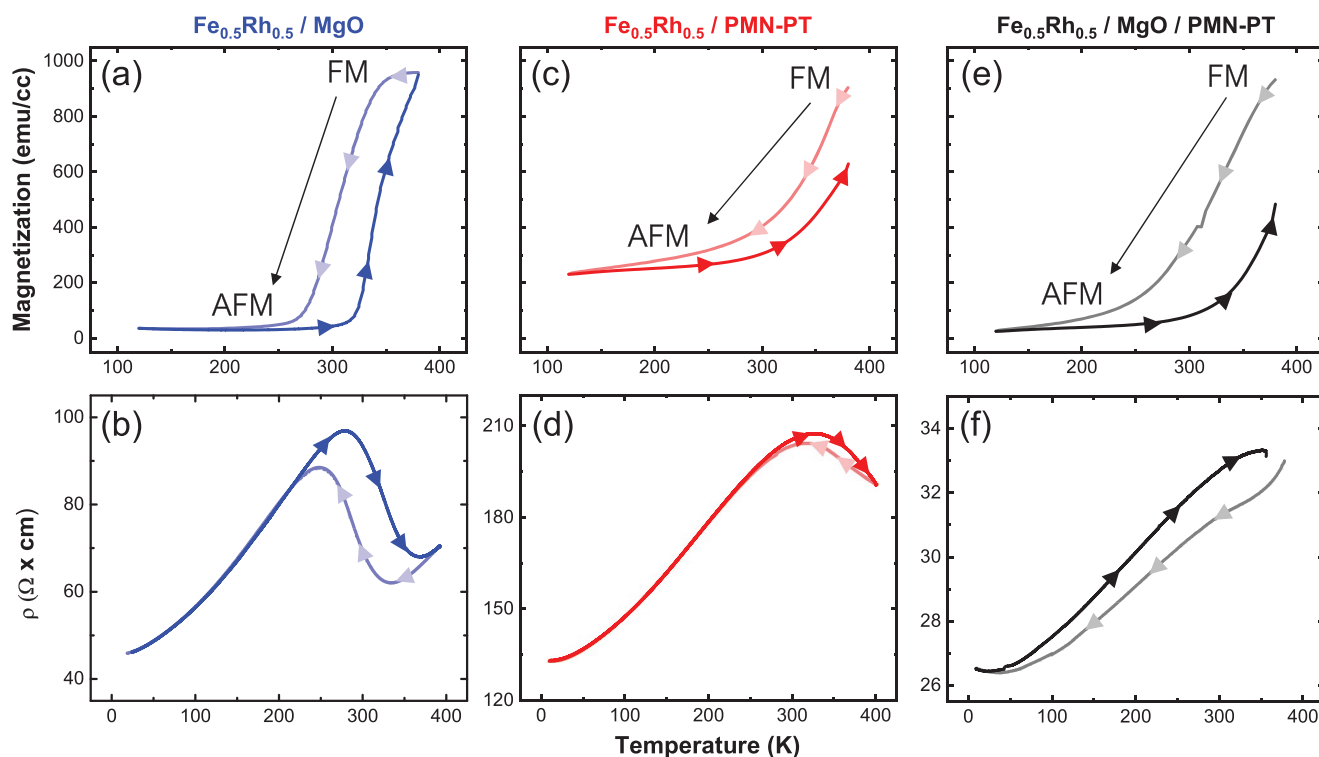


Figure 2. Magnetization and resistivity data as a function of temperature for the as-grown heterostructures, including a) magnetization and b) transport data for the Fe_{0.5}Rh_{0.5}/MgO heterostructures, c) magnetization and d) transport data for the Fe_{0.5}Rh_{0.5}/PMN-PT heterostructures, and e) magnetization and f) transport data for the Fe_{0.5}Rh_{0.5}/MgO/PMN-PT heterostructures.

reveal an additional ferromagnetic phase contribution, as indicated by the non-zero magnetization value observed at low temperatures (<250 K), the wide temperature range of the phase transition, and an enhanced mid-point temperature for the transition (Figure 2c). This further suppresses the difference between the resistivity of the two states (Figure 2d). Finally, for the Fe_{0.5}Rh_{0.5}/MgO/PMN-PT heterostructures, there is a (partial) improvement of the properties compared to the Fe_{0.5}Rh_{0.5}/PMN-PT heterostructures (Figure 2e,f). While the width of the phase transition (hysteresis) is still quite broadened and the mid-point temperature for the transition is increased, the magnetization does reach zero at low temperatures; suggesting an improved crystalline quality for the Fe_{0.5}Rh_{0.5} upon inclusion of the MgO-buffer layer. Nonetheless, the resistivity behavior is less clean than for films grown directly on MgO substrates.

The magnetic quality of the Fe_{0.5}Rh_{0.5} is only one part of the challenge. For the magnetoelectric function to be produced we must be able to apply electric fields to the piezoelectric PMN-PT and produce strains that drive changes in the magnetization. To gauge how the Fe_{0.5}Rh_{0.5} deposition process (high temperature, low oxygen pressure) impacts the PMN-PT we probed the room-temperature leakage behavior of several heterostructure types (Experimental Section and Figure S5, Supporting Information). For the Fe_{0.5}Rh_{0.5}/PMN-PT heterostructures, large and (fairly) symmetric leakage current-voltage behavior is observed. This is consistent with the diminished magnetization data for these same heterostructures and points to the fact that the high-temperature and reducing growth environment for the Fe_{0.5}Rh_{0.5} likely results in the oxidation of the Fe_{0.5}Rh_{0.5} and degradation of the PMN-PT that ultimately limits the utility of these heterostructures. This is made more obvious by comparing a test structure of room-temperature deposited platinum as the top contacts to the PMN-PT which show considerably lower leakage current densities, especially under negative bias (applying voltage from the top metal layer to the bottom Ba_{0.5}Sr_{0.5}RuO₃). Such structures also show highly asymmetric leakage profiles which is due to the asymmetry of the top metal (platinum) and bottom Ba_{0.5}Sr_{0.5}RuO₃ electrodes. To address this, the MgO-buffer layer was explored to address this potential challenge and leakage studies of the Fe_{0.5}Rh_{0.5}/MgO/PMN-PT heterostructures reveal responses more akin to those of the Pt/PMN-PT structures; in other words, the thin insulating MgO likely suppress the oxidation of the Fe_{0.5}Rh_{0.5} and the degradation of the PMN-PT during the subsequent high-temperature Fe_{0.5}Rh_{0.5} growth. In all, these studies of crystal structure and structural quality, magnetic properties of the Fe_{0.5}Rh_{0.5}, and leakage behavior of the devices suggest that it is possible to produce high-quality, epitaxial Fe_{0.5}Rh_{0.5} thin films on PMN-PT thin films and that the inclusion of a thin MgO layer both improves the Fe_{0.5}Rh_{0.5} quality and suppresses degradation of the PMN-PT films during high-temperature, low-pressure Fe_{0.5}Rh_{0.5} growth.

Having established the quality of the Fe_{0.5}Rh_{0.5}/MgO and Fe_{0.5}Rh_{0.5}/MgO/PMN-PT heterostructures, we focus on these two heterostructure types as we explore methodologies to probe magnetoelectric coupling in micron-scale devices. Since the Fe_{0.5}Rh_{0.5} simultaneously serves as the active magnetic layer and the top electrode it must be defined into small device sizes, thus making use of traditional magnetic probes (such

as magnetometry) challenging. Alternatively, we can leverage magnetotransport approaches and especially the anomalous Hall effect (AHE) to probe the magnetoelectric coupling instead of relying on direct measurements of magnetization under applied electric fields. To probe the AHE, the Fe_{0.5}Rh_{0.5}/MgO and Fe_{0.5}Rh_{0.5}/MgO/PMN-PT heterostructures were fabricated into Hall bars (~5 μm x 15 μm in size; Experimental Section and Figure 3a). Before quantifying the magnetoelectric coupling, we first measured temperature-dependent AHE curves of the Fe_{0.5}Rh_{0.5}/MgO (Figure 3b) and Fe_{0.5}Rh_{0.5}/MgO/PMN-PT (Figure 3c) heterostructures. The Fe_{0.5}Rh_{0.5}/MgO heterostructures serve as a reference for the AHE changes during the AFM-to-FM phase transition in Fe_{0.5}Rh_{0.5}. At 250 K, the Fe_{0.5}Rh_{0.5} in both heterostructures is in the pure AFM phase with negligible magnetization and, hence, the ordinary Hall effect dominates the transport. As the temperature increases, the Hall resistivity (ρ_{xy}) of the Fe_{0.5}Rh_{0.5} becomes dominated by contributions from the AHE, which indicates that the AFM-to-FM phase transition has been initiated upon increasing temperature. As a result, ρ_{xy} increases with magnetic field and falls back with decreasing magnetic field. Both the Fe_{0.5}Rh_{0.5}/MgO and Fe_{0.5}Rh_{0.5}/MgO/PMN-PT heterostructures behave similarly in nature, but with the temperature for the onset of and completion of the AFM-to-FM transition being higher in the Fe_{0.5}Rh_{0.5}/MgO/PMN-PT heterostructure.

As it pertains to the magnetoelectric coupling, the ultimate goal is to produce a quantitative estimate of the magnetoelectric coupling coefficient $\alpha_{ME} = \mu_0 \frac{\Delta M}{E}$ where M is the magnetization and E is the applied electric field. While E can be readily understood from the applied voltage and device geometry, the estimation of ΔM poses a challenge due to the lack of direct measurements of magnetization in the small volume/area devices. To overcome this challenge, we leveraged the linear temperature-dependence of the spin-flop field (SFF, the magnetic field at which a spin-flop transition occurs) extracted from the temperature-dependent Hall-resistivity studies (Figure 3d). Again, the nature of the two heterostructures is the same with nearly identical slopes for the response with varying temperature. Therefore, we can use this information to estimate the ΔM value under a given E by first finding the temperature which is expected to have the same SFF as the SFF under the applied E. In turn, the difference in temperature is then converted to an estimated ΔM using the magnetization-temperature curves from the same heterostructures (Figure 2).

To quantify α_{ME} , negative voltages were applied to the Fe_{0.5}Rh_{0.5}/MgO/PMN-PT heterostructures and the resultant magnetotransport was measured at 325 K (Experimental Section, Figure 4a). Of course, there is no effect in the Fe_{0.5}Rh_{0.5}/MgO heterostructures and similar experiments were tried for the Fe_{0.5}Rh_{0.5}/PMN-PT, but the large leakage effects limited their utility (Figure S6, Supporting Information). The ρ_{xy} curves reveal signs of voltage dependence, in which the SFF increases with increasing magnitude of applied voltage (Figure 4a). This indicates that the AFM-to-FM phase transition occurs at different fields under applied voltage. Observable changes in AHE can even be seen at -0.5 V (-50 kV cm⁻¹), which saturate at -0.75 V (-75 kV cm⁻¹). Using the aforementioned linear relationship between SFF and temperature (Figure 3d), the SFF

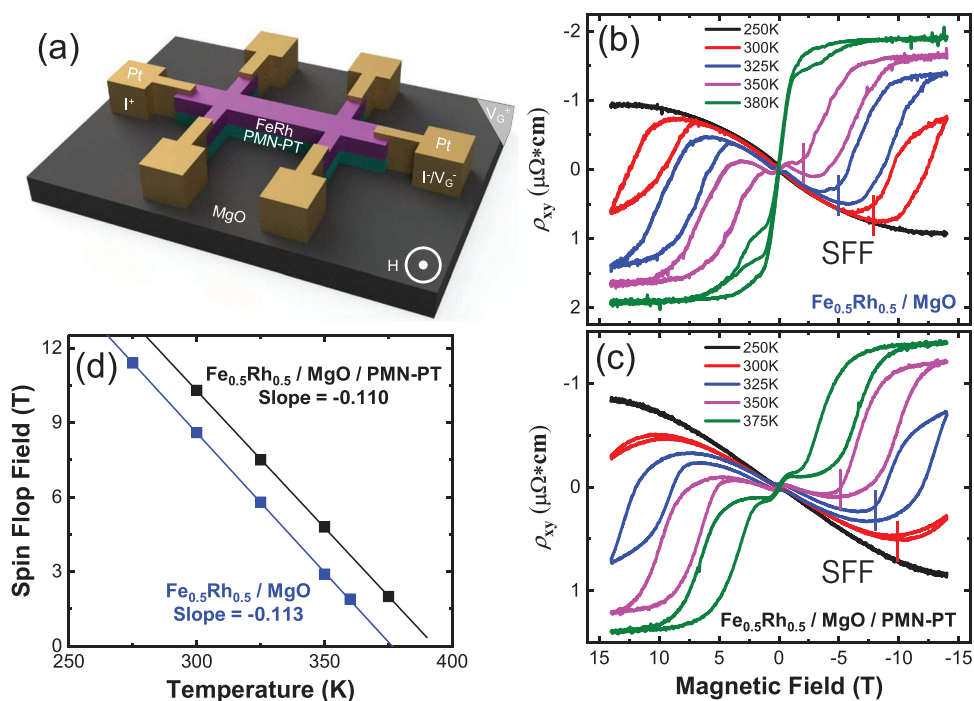


Figure 3. a) Schematic illustration of the Hall-bar devices fabricated into the various heterostructures. Anomalous Hall resistivity as a function of applied magnetic field at various temperatures for the b) $\text{Fe}_{0.5}\text{Rh}_{0.5}/\text{MgO}$ and c) $\text{Fe}_{0.5}\text{Rh}_{0.5}/\text{MgO}/\text{PMN-PT}$ heterostructures. d) Summary of the spin flop field (SFF) as a function of temperature for the different heterostructure variants revealing similar temperature-dependence for both heterostructures.

changes at 325 K for the $\text{Fe}_{0.5}\text{Rh}_{0.5}/\text{MgO}/\text{PMN-PT}$ heterostructures under different voltages are used to estimate the temperature at which the $\text{Fe}_{0.5}\text{Rh}_{0.5}$ has the same SFF. The difference

between the magnetization at this temperature and the magnetization at 325 K (ΔM) is then extracted from the magnetization-temperature curves (Figure 2e); a summary of the

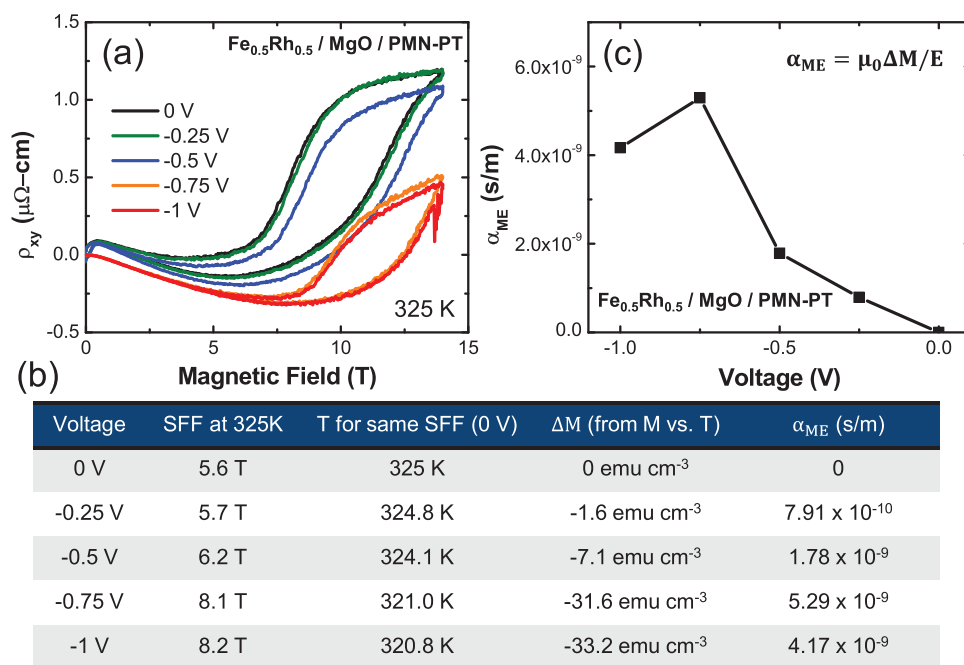


Figure 4. a) Anomalous Hall resistivity as a function of magnetic field measured at different applied dc voltages for the $\text{Fe}_{0.5}\text{Rh}_{0.5}/\text{MgO}/\text{PMN-PT}$ heterostructures reveals a strong magnetoelectric effect with a sharp raise in magnitude between -0.5 and -0.75 V. b) Summary of important values from both the magnetization and transport studies to estimate the magnetoelectric coupling. c) Evolution of the magnetoelectric coupling coefficient α_{ME} as a function of applied voltage in this system.

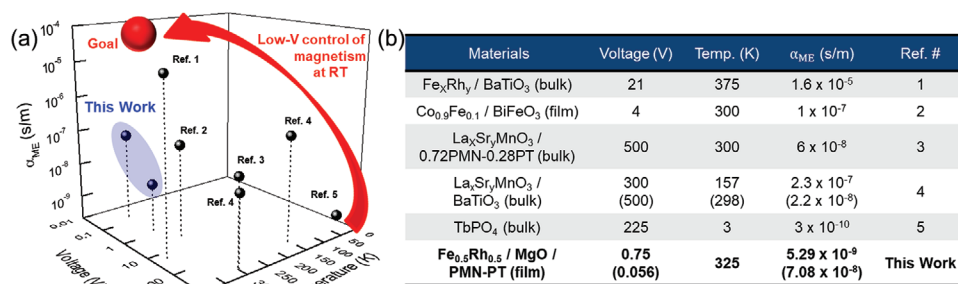


Figure 5. a) Graphical and b) table summary of studies of magnetoelectric coupling coefficient α_{ME} in ferromagnetic/piezoelectric-ferroelectric heterostructures (including both bulk and thin-film forms). The ultimate goal is to achieve ultralow energy (~ 1 aJ = 1×10^{-18} J) per operation in scaled magnetoelectric devices near the room temperature. For a scaled device area of 100 nm^2 , a coercive voltage of 100 mV corresponds to ~ 1 aJ per cycle of the material/device, a value which is still stable against thermal fluctuation at room-temperature ($\sim 26 \text{ meV}$). Pertinent references include: 1) R. Cherifi, et al. *Nature Mater.* **13**, 345–351 (2014); 2) J. Heron, et al. *Nature* **516**, 370–373 (2014); 3) C. Thiele, et al. *Phys. Rev. B* **75**, 05 4408 (2007); 4) W. Eerenstein, et al. *Nature Mater.* **6**, 348–351 (2007); and 5) G. T. Rado, et al. *Phys. Rev. B* **29**, 4041 (1984).

pertinent values of important terms (i.e., applied voltage, SFF at 325 K, the equivalent temperature for the same SFF at 0 V, the estimated ΔM , and the extracted α_{ME}) are provided in a table (Figure 4b). The extracted $\alpha_{ME} = \mu_0 \frac{\Delta M}{E}$ as a function of negative voltage shows a sharp increase between -0.5 and -0.75 V and reaches a value of $5.29 \times 10^{-9} \text{ s m}^{-1}$ at 325 K at the maximum (Figure 4c). At higher voltages, further changes in the AHE are not observed, likely due to the potential leakage at high electric fields and/or saturation of the piezoelectric strain of the films.

The observed values of α_{ME} can be compared to prior works on bulk crystals and thin films (Figure 5). Ideally, the combination of low voltage ($<100 \text{ mV}$) actuation, room-temperature (300 K) functionality, and resulting large α_{ME} characteristics (approaching the red point in Figure 5a) are desired. As the large scatter in the data suggests, however, this is a challenging task. Although $Fe_{0.5}Rh_{0.5}/MgO/PMN-PT$ heterostructures satisfy the low voltage (-0.75 V) and near room-temperature (325 K) characteristics, they suffer from relatively small α_{ME} . This is likely caused by the reduced piezoelectric strains in clamped films^[37] and due to the thin (relatively lower dielectric constant) MgO-buffer layer (to address issues in integrating the $Fe_{0.5}Rh_{0.5}$ with PMN-PT). To evaluate the potential of further improvements in thin films, we estimate the effective α_{ME} based on the actual voltage drop across the PMN-PT layer. Here, the actual voltage drops in MgO (dielectric permittivity of 8) and PMN-PT (dielectric permittivity of 1000) layer can be estimated from charge continuity conditions at the interface.^[35] Using these values, when -0.75 V is applied to the device, the voltage drops across the MgO and PMN-PT layers are estimated to be -0.694 V and -0.056 V , respectively. Using this rather simple estimation, one obtains an effective α_{ME} of $7.08 \times 10^{-8} \text{ s m}^{-1}$ at 325 K, which is comparable to the α_{ME} obtained using single-crystal $BaTiO_3$ and $0.72PMN-0.28PT$ substrates (Figure 5b).^[38,39] We expect that the fabrication of laterally defined structures (thereby removing some of the in-plane clamping of the films), the integration of piezoelectric membranes released from the substrate,^[40,41] and improvements in the growth process^[42] can lead to further enhancement of the magnetoelectric response.

3. Conclusion

In summary, it has been shown that it is possible to translate similar magnetoelectric heterostructures studied in the bulk to the thin-film regime. It is possible to produce high-quality, epitaxial, (001)-oriented films of $Fe_{0.5}Rh_{0.5}$ on PMN-PT and MgO/PMN-PT thin films. Subsequent temperature-dependent magnetization and resistivity studies reveal the ability to produce near-room-temperature phase transitions in the $Fe_{0.5}Rh_{0.5}$. A methodology to probe and quantify the magnetoelectric coupling in small thin-film devices via AHE studies was also developed wherein one can compare the SFF change induced by temperature and external voltage to extract a measure of α_{ME} . Using this approach, α_{ME} was estimated to be $5.29 \times 10^{-9} \text{ s m}^{-1}$ at 325 K under -0.75 V and as large as $7.08 \times 10^{-8} \text{ s m}^{-1}$ if one accounts only for the voltage drop across the PMN-PT. While this is promising for next-generation electric-field control of magnetization, improvements in integration of the dissimilar materials and the nanofabrication approaches are necessary to further enlarge piezoelectric responses in thin films.

4. Experimental Section/Methods

Epitaxial Thin-film Synthesis: Pulsed-laser deposition (PLD) using a KrF excimer laser (248 nm, LPX 300, Coherent) was used to grow $100 \text{ nm } 0.68Pb(Mg_{1/3}Nb_{2/3})O_3-0.32PbTiO_3$ (PMN-PT) / $25 \text{ nm } Ba_{0.5}Sr_{0.5}RuO_3$ (BSRO) heterostructures on $NdScO_3$ (NSO) (110) substrates (CrysTec GmbH). The PMN-PT growth was carried out at a heater temperature of $600 \text{ }^\circ\text{C}$ in a dynamic oxygen pressure of 200 mTorr with a laser fluence of 1.8 J cm^{-2} and a laser repetition rate of 2 Hz from a ceramic target (Praxair) of the same composition with 10% lead excess to compensate for lead loss during growth. The BSRO growth was carried out at temperature of $750 \text{ }^\circ\text{C}$ in a dynamic oxygen pressure of 20 mTorr with a laser fluence of 1.85 J cm^{-2} and a laser repetition rate of 3 Hz from a ceramic target (Praxair) of the same composition. Following the growth, the samples were cooled to room temperature at $5 \text{ }^\circ\text{C min}^{-1}$ in a static oxygen pressure of 700 Torr. In the case of MgO-buffered heterostructures, 3–10 nm MgO buffer layer was grown by PLD immediately after PMN-PT at the PMN-PT growth temperature of $600 \text{ }^\circ\text{C}$ in a dynamic oxygen pressure of 20 mTorr with a laser fluence of 2.5 J cm^{-2} and a laser repetition rate of 15 Hz from a

ceramic target (Praxair) of the same composition. $\text{Fe}_{0.5}\text{Rh}_{0.5}$ films were grown using DC sputtering techniques. For the sputtering deposition of $\text{Fe}_{0.5}\text{Rh}_{0.5}$, the PMN-PT / BSRO / NSO heterostructures were heated to 500–700 °C in a base pressure of at least 10^{-8} Torr. Subsequently, a small amount of argon gas was introduced into the chamber, maintaining the total pressure at 3 mTorr. The $\text{Fe}_{0.5}\text{Rh}_{0.5}$ films were then grown from a stoichiometric $\text{Fe}_{0.5}\text{Rh}_{0.5}$ target. After the deposition, films were annealed at various temperatures between 600 and 800 °C in vacuum for 40 min. and subsequently cooled to room temperature at 10 °C min^{-1} . 3 nm thick capping platinum layers were also grown by DC sputtering at room-temperature and a target power of 100 W in a dynamic argone pressure of 2 mTorr to prevent the oxidation of FeRh.

Structural Characterization: X-ray θ - 2θ line scans about symmetrical reflections of the films and substrates were conducted with a high-resolution X-ray diffractometer (X'pert Pro2, PANalytical).

Magnetometry: Magnetic characterizations were carried out with a superconducting quantum interference device magnetometer (Quantum Design, 2 K, 7 T), with the magnetic field applied along the out-of-plane direction of the film.

Transport Measurements: The temperature-dependent resistance and Hall effect measurement were carried out in a CRYOGENIC measurement system (2 K, 14 T) with the magnetic field applied perpendicular to the device plane. A constant 10 μA DC current was applied for all temperature-dependent resistivity measurements. A constant 100 μA DC current was applied for all Hall measurements with a series of back gating voltages.

Device Fabrication for AHE Studies: To measure the physical properties of the $\text{Fe}_{0.5}\text{Rh}_{0.5}$ / (MgO) / PMN-PT heterostructures, the active region was patterned into a 6-point contact Hall bar geometry (20 $\mu\text{m} \times$ 400 μm) by the following fabrication process. First, photoresist was patterned by spin-coating on the blanket Pt / $\text{Fe}_{0.5}\text{Rh}_{0.5}$ / (MgO) / PMN-PT heterostructures. Second, the photoresist was patterned into Hall-bar geometries via standard optical photolithography. Third, the heterostructures were ion-milled to define the active region. Fourth, a 300-nm-thick insulating layer of MgO was deposited at room-temperature by PLD to separate the bottom contacts from the top contacts. Fifth, the photoresist was removed in acetone and a second photoresist layer was spin-coated for the second photolithography step. Sixth, inverse patterns of platinum contact pads were formed by photolithography. Seventh, a 100-nm-thick layer of platinum was deposited to form contact pads. Eighth, the photoresist was removed in acetone. Ninth, the heterostructures were mounted on a chip carrier and wire-bonded for insertion in the measurement system.

Supporting Information

Supporting Information is available from the Wiley Online Library or from the author.

Acknowledgements

W.Z. and J.K. contributed equally to the work. W.Z., J.K., and L.W.M. acknowledge the Intel Corp. via the FEINMAN program. X.H and R.R. acknowledge the support of ASCENT, one of the SRC-JUMP Centers. D.P. acknowledges funding from the European Union's Horizon 2020 research and innovation program under the Marie Skłodowska-Curie grant agreement No. 79712. G.A.P.V. acknowledges support from the National Science Foundation under grant DMR-1708615 and from the NSF GRFP.

Conflict of Interest

The authors declare no conflict of interest.

Data Availability Statement

The data that support the findings of this study are available from the corresponding author upon reasonable request.

Keywords

anomalous Hall effect, magnetoelectric coupling, multiferroic heterostructures, nonvolatile, piezo-strain effect

Received: May 27, 2021

Revised: June 28, 2021

Published online: July 9, 2021

- [1] G. E. Moore, *P. IEEE* **1998**, *86*, 82.
- [2] R. H. Dennard, F. H. Gaensslen, H.-N. Yu, V. L. Rideout, E. Bassous, A. R. Leblanc, *P. IEEE* **1999**, *87*, 668.
- [3] H. N. Khan, D. A. Hounshell, E. R. H. Fuchs, *Nat. Electron.* **2018**, *1*, 14.
- [4] D. E. Nikonov, I. A. Young, *IEEE J. Explor. S. Comput. Dev. Circ.* **2015**, *1*, 3.
- [5] S. Manipatruni, D. E. Nikonov, I. A. Young, *Nat. Phys.* **2018**, *14*, 338.
- [6] D. E. Nikonov, I. A. Young, *P. IEEE* **2013**, *101*, 2498.
- [7] D. E. Nikonov, G. I. Bourianoff, T. Ghani, *IEEE Electr. Device L* **2011**, *32*, 1128.
- [8] B. Behin-Aein, D. Datta, S. Salahuddin, S. Datta, *Nat. Nanotechnol.* **2010**, *5*, 266.
- [9] A. Imre, G. Csaba, L. Ji, A. Orlov, G. H. Bernstein, W. Porod, *Science* **2006**, *311*, 205.
- [10] U. E. Avci, R. Rios, K. Kuhn, I. A. Young, 2011 Symposium on VLSI Technology Digest of Technical Papers, **2011**.
- [11] A. M. Ionescu, H. Riel, *Nature* **2011**, *479*, 329.
- [12] S. Salahuddin, S. Datta, *Nano Lett.* **2008**, *8*, 405.
- [13] D. Newns, B. Elmegreen, X. H. Liu, G. Martyna, *J. Appl. Phys.* **2012**, *111*, 084509.
- [14] S. Salahuddin, K. Ni, S. Datta, *Nat. Electron.* **2018**, *1*, 442.
- [15] V. Calayir, D. E. Nikonov, S. Manipatruni, I. A. Young, *IEEE T. Circ. Syst. Regul. Pap.* **2014**, *61*, 393.
- [16] F. Hellman, A. Hoffmann, Y. Tserkovnyak, G. S. D. Beach, E. E. Fullerton, C. Leighton, A. H. MacDonald, D. C. Ralph, D. A. Arena, H. A. Dürr, P. Fischer, J. Grollier, J. P. Heremans, T. Jungwirth, A. V. Kimel, B. Koopmans, I. N. Krivorotov, S. J. May, A. K. Petford-Long, J. M. Rondinelli, N. Samarth, I. K. Schuller, A. N. Slavin, M. D. Stiles, O. Tchernyshyov, A. Thiaville, B. L. Zink, *Rev. Mod. Phys.* **2017**, *89*, 025006.
- [17] S. Manipatruni, D. E. Nikonov, C.-C. Lin, T. A. Gosavi, H. Liu, B. Prasad, Y.-L. Huang, E. Bonturim, R. Ramesh, I. A. Young, *Nature* **2019**, *565*, 35.
- [18] R. O. Cherifi, V. Ivanovskaya, L. C. Phillips, A. Zobelli, I. C. Infante, E. Jacquet, V. Garcia, S. Fusil, P. R. Bridson, N. Guiblin, A. Mougín, A. A. Ünal, F. Kronast, S. Valencia, B. Dkhil, A. Barthélémy, M. Bibes, *Nat. Mater.* **2014**, *13*, 345.
- [19] S. Zhang, Y. G. Zhao, P. S. Li, J. J. Yang, S. Rizwan, J. X. Zhang, J. Seidel, T. L. Qu, Y. J. Yang, Z. L. Luo, Q. He, T. Zou, Q. P. Chen, J. W. Wang, L. F. Yang, Y. Sun, Y. Z. Wu, X. Xiao, X. F. Jin, J. Huang, C. Gao, X. F. Han, R. Ramesh, *Phys. Rev. Lett.* **2011**, *108*, 137203.
- [20] X. He, Y. Wang, N. Wu, A. N. Caruso, E. Vescovo, K. D. Belashchenko, P. A. Dowben, C. Binek, *Nat. Mater.* **2010**, *9*, 579.
- [21] J. T. Heron, J. L. Bosse, Q. He, Y. Gao, M. Trassin, L. Ye, J. D. Clarkson, C. Wang, J. Liu, S. Salahuddin, D. C. Ralph, D. G. Schlom, J. Íñiguez, B. D. Huey, R. Ramesh, *Nature* **2014**, *516*, 370.

- [22] Y. Lee, Z. Q. Liu, J. T. Heron, J. D. Clarkson, J. Hong, C. Ko, M. D. Biegalski, U. Aschauer, S. L. Hsu, M. E. Nowakowski, J. Wu, H. M. Christen, S. Salahuddin, J. B. Bokor, N. A. Spaldin, D. G. Schlom, R. Ramesh, *Nat. Commun.* **2015**, *6*, 5959.
- [23] R. L. Conte, J. Gorchon, A. Mougin, C. H. A. Lambert, A. El-Ghazaly, A. Scholl, S. Salahuddin, J. Bokor, *Phys. Rev. Mater.* **2018**, *2*, 091402.
- [24] N. A. Spaldin, M. Fiebig, *Science* **2005**, *309*, 391.
- [25] M. Fiebig, *J. Phys. D Appl. Phys.* **2005**, *38*, R123.
- [26] W. Zhao, D. Zhang, D. Meng, W. Huang, L. Feng, C. Hou, Y. Lu, Y. Yin, X. Li, *Appl. Phys. Lett.* **2016**, *109*, 263502.
- [27] S. Yang, R. Peng, T. Jiang, Y. Liu, L. Feng, J. Wang, L. Chen, X. Li, C. Nan, *Adv. Mater.* **2014**, *26*, 7091.
- [28] S. Yang, L. Feng, D. Zhang, W. Huang, S. Dong, J. Wang, L. Zou, X. Li, C. Nan, *J. Alloy. Compd.* **2015**, *646*, 472.
- [29] S. Zhang, Y. Zhao, X. Xiao, Y. Wu, S. Rizwan, L. Yang, P. Li, J. Wang, M. Zhu, H. Zhang, X. Jin, X. Han, *Sci. Rep.* **2014**, *4*, 3727.
- [30] Y. Cheng, B. Peng, Z. Hu, Z. Zhou, M. Liu, *Phys. Lett. A* **2018**, *382*, 3018.
- [31] L. J. Swartzendruber, *B. Alloy P. Diag.* **1984**, *5*, 456.
- [32] V. L. Moruzzi, P. M. Marcus, *Phys. Rev. B* **1992**, *46*, 2864.
- [33] I. Suzuki, T. Naito, M. Itoh, T. Sato, T. Taniyama, *J. Appl. Phys.* **2011**, *109*, 07C717.
- [34] J. Kim, S. Saremi, M. Acharya, G. Velarde, E. Parsonnet, P. Donahue, A. Qualls, D. Garcia, L. W. Martin, *Science* **2020**, *369*, 81.
- [35] J. Kim, H. Takenaka, Y. Qi, A. R. Damodaran, A. Fernandez, R. Gao, M. R. McCarter, S. Saremi, L. Chung, A. M. Rappe, L. W. Martin, *Adv. Mater.* **2019**, *31*, 1901060.
- [36] D. Kande, S. Pisana, D. Weller, D. E. Laughlin, J.-G. Zhu, *IEEE T. Magn* **2011**, *47*, 3296.
- [37] V. Nagarajan, C. S. Ganpule, B. Nagaraj, S. Aggarwal, S. P. Alpay, A. L. Roytburd, E. D. Williams, R. Ramesh, *Appl. Phys. Lett.* **1999**, *75*, 4183.
- [38] W. Eerenstein, M. Wiora, J. L. Prieto, J. F. Scott, N. D. Mathur, *Nat. Mater.* **2007**, *6*, 348.
- [39] C. Thiele, K. Dörr, O. Bilani, J. Rödel, L. Schultz, *Phys. Rev. B* **2007**, *75*, 054408.
- [40] H. S. Kum, H. Lee, S. Kim, S. Lindemann, W. Kong, K. Qiao, P. Chen, J. Irwin, J. H. Lee, S. Xie, S. Subramanian, J. Shim, S.-H. Bae, C. Choi, L. Ranno, S. Seo, S. Lee, J. Bauer, H. Li, K. Lee, J. A. Robinson, C. A. Ross, D. G. Schlom, M. S. Rzchowski, C.-B. Eom, J. Kim, *Nature* **2020**, *578*, 75.
- [41] D. Pesquera, E. Parsonnet, A. Qualls, R. Xu, A. J. Gubser, J. Kim, Y. Jiang, G. Velarde, Y. Huang, H. Y. Hwang, R. Ramesh, L. W. Martin, *Adv. Mater.* **2020**, *32*, 2003780.
- [42] S. H. Baek, J. Park, D. M. Kim, V. A. Aksyuk, R. R. Das, S. D. Bu, D. A. Felker, J. Lettieri, V. Vaithyanathan, S. S. N. Bharadwaja, N. Bassiri-Gharb, Y. B. Chen, H. P. Sun, C. M. Folkman, H. W. Jang, D. J. Kreft, S. K. Streiffer, R. Ramesh, X. Q. Pan, S. Trolier-McKinstry, D. G. Schlom, M. S. Rzchowski, R. H. Blick, C. B. Eom, *Science* **2011**, *334*, 958.